

# TokaMind: A Multi-Modal Transformer Foundation Model for Tokamak Plasma Dynamics

Tobia Boschi  
IBM Research Europe  
Dublin, Ireland  
tobia.boschi@ibm.com

Rodrigo H. Ordóñez-Hurtado  
IBM Research Europe  
Dublin, Ireland  
rodrigo.ordonez.hurtado@ibm.com

Eszter Székely  
UK Atomic Energy Authority  
Abingdon, UK  
eszter.szekely@ukaea.uk

Adriano Agnello  
STFC Hartree Centre  
Daresbury, UK  
adriano.agnello@stfc.ac.uk

Robert Akers  
UK Atomic Energy Authority  
Abingdon, UK  
rob.akers@ukaea.uk

Andrea Loreti  
UK Atomic Energy Authority  
Abingdon, UK  
andrea.loreti@ukaea.uk

Cécile Rousseau  
IBM Research Europe  
Dublin, Ireland  
rousseau.cecile@ibm.com

Alexander Whittle  
UK Atomic Energy Authority  
Abingdon, UK  
alexander.whittle@ukaea.uk

Stanislas Pamela  
UK Atomic Energy Authority  
Abingdon, UK  
Stanislas.Pamela@ukaea.uk

Juan Bernabe Moreno  
IBM Research Europe  
Dublin, Ireland  
juan.bernabe-moreno@ibm.com

Mykhaylo Zayats  
IBM Research Europe  
Dublin, Ireland  
mykhaylo.zayats1@ibm.com

Nicola C. Amorisco  
UK Atomic Energy Authority  
Abingdon, UK  
nicola.amorisco@ukaea.uk

George K. Holt  
STFC Hartree Centre  
Daresbury, UK  
george.holt@stfc.ac.uk

Samuel Jackson  
UK Atomic Energy Authority  
Abingdon, UK  
samuel.jackson@ukaea.uk

Alessandra Pascale  
IBM Research Europe  
Dublin, Ireland  
apascale@ie.ibm.com

Vassil Alexandrov  
STFC Hartree Centre  
Daresbury, UK  
vassil.alexandrov@stfc.ac.uk

## Abstract

We present **TOKAMIND**, an open-source foundation model framework for fusion plasma modeling, based on a Multi-Modal Transformer (MMT) and trained on heterogeneous tokamak diagnostics from the publicly available MAST dataset. **TOKAMIND** supports multiple data modalities (time-series, 2D profiles, and videos) with different sampling rates, robust missing-signal handling, and efficient task adaptation via selectively loading and freezing four model components. To represent multi-modal signals, we use a training-free Discrete Cosine Transform embedding (DCT3D) and provide a clean interface for alternative embeddings (e.g., Variational Autoencoders - VAEs). We evaluate **TOKAMIND** on the recently introduced MAST benchmark **TOKAMARK**, comparing training and embedding strategies. Our results show that fine-tuned TokaMind outperforms the benchmark baseline on all but one task, and that, for several tasks, lightweight fine-tuning yields better performance than training the same architecture from scratch under a matched epoch budget. These findings highlight the benefits of multi-modal pre-training for tokamak plasma dynamics and provide a practical,

extensible foundation for future fusion modeling tasks. Training code and model weights will be made publicly available.

## Keywords

Multi-modal Transformer, Foundation Models, Tokamak, Fusion Energy, Plasma Dynamics

## 1 Introduction

*Fusion energy and tokamak operation.* Magnetic-confinement fusion aims to produce abundant, low-carbon energy by sustaining high-temperature plasmas under tight stability and safety constraints [22]. Among leading reactor concepts, tokamaks are a prominent design, but achieving reliable, high-performance operation depends on accurate reconstruction and forecasting of plasma behavior, which underpins monitoring and, ultimately, control across operating regimes [6]. Recent national roadmaps such as the Fusion Science & Technology Roadmap [20] emphasize accelerating progress toward a demonstration of a practical fusion power plant by advancing integrated modeling and AI-enabled, data-driven methods for plasma analysis and prediction.

*Tokamak data challenges.* Tokamak experiments are governed by strongly-coupled, nonlinear plasma dynamics [1] and produce heterogeneous signals spanning multiple modalities and time scales (e.g., scalar time-series, structured profiles, and imaging). Because the plasma state is not directly observable, it must be inferred from indirect and noisy measurements [5]. This makes reconstruction and forecasting intrinsically challenging and often ill-posed, particularly when diagnostic availability varies across shots or operating regimes [14]. Beyond reconstruction of the instantaneous plasma state, modeling plasma evolution also requires actuator information (e.g., fueling commands and voltages applied by power supplies), which provides essential context for how the system is driven [8]. Finally, experimental datasets commonly include missing channels and dropouts and induce task-dependent input/output sets, posing a practical challenge for methods trained on real experimental records [13].

*Current approaches and limitations.* The above challenges have motivated growing interest in data-driven pipelines that complement physics-based tools and accelerate analysis and control in practical experimental settings [10]. Recent Machine Learning approaches have demonstrated promising performance on targeted reconstruction and control-oriented tasks [15, 19], typically by learning mappings from a selected set of diagnostic inputs (and sometimes actuators) to task-specific outputs. However, many existing models are specialized to a particular objective, time horizon, and curated signal set, and assume fixed input/output schemas and consistent diagnostic availability [23]. This specialization limits reuse across tasks with different targets, reduces robustness to missing channels and dropouts, and hinders transfer to new devices or operating regimes. In short, we require more generalist approaches that (i) learn transferable representations of plasma dynamics directly from heterogeneous data, (ii) support a wide range of downstream objectives with minimal task-specific adaptation, and (iii) generalize across devices and operating regimes, particularly in low-data settings.

*Foundation models for plasma dynamics.* A natural way to address these constraints is to move from task-specific models to *foundation models* (FMs): models *pretrained* on broad, heterogeneous data and objectives so that a single initialization can be efficiently adapted to many downstream tasks and changing signal schemas [2, 7]. In this paradigm, pretraining aims to learn transferable representations that reduce the amount of task-specific data and tuning required, and can improve robustness under changing inputs, targets, and operating conditions. In fusion, early perspectives have begun to articulate how FM-style pretraining could support experimental workflows [4]. The adoption of domain-specific FMs is increasingly practical also thanks to open data infrastructure and standardized benchmarks: FAIR-MAST provides access to MAST data, while TOKAMARK standardizes multi-task evaluation [11, 12, 18].

*TokaMind: a multi-modal transformer FM for fusion plasma.* Motivated by the need for transferable, schema-flexible models of plasma dynamics, we introduce **TOKAMIND**, an open-source FM framework for fusion plasma modeling based on a **Multi-Modal Transformer (MMT)** *pretrained* on the MAST dataset [11, 12]. Through

broad multi-signal pretraining, TOKAMIND yields a reusable initialization that can be efficiently adapted to new tasks and changing input/output schemas. Efficient codec-based signal compression, coupled with a modular design, yields a lightweight model (< 10M parameters) that supports heterogeneous modalities and time scales under changing signal availability.

Our main contributions are:

- **A schema-flexible, multi-modal transformer framework** for tokamak data (time-series, profiles, and videos) with robust missing-signal handling.
- **A modular tokenization and codec interface** that converts windowed multi-rate signals into a variable-length set of tokens via chunking and modality-aware embeddings, with a strong default training-free DCT3D codec and clean hooks for learned alternatives (e.g., Variational Autoencoders - VAEs).
- **Efficient adaptation mechanisms** (warm-start + selective freezing) that reuse pretrained components across tasks with diverse objectives.
- **Benchmark validation**, showing consistent improvements over a CNN baseline across nearly all tasks. Warm-start finetuning also yields clear gains over training the same architecture from scratch, particularly in the most challenging regimes—supporting the value of transferable representations of plasma dynamics.

*Evaluation settings.* We validate TOKAMIND on TOKAMARK [18], a standardized benchmark on MAST, which formalizes task definitions, preprocessing, and evaluation, and provides a strong CNN baseline for comparison.

*Paper outline.* The remainder of the paper is organized as follows. Section 2 summarizes the benchmark setting; Section 3 describes the TOKAMIND tokenizer and embedding codecs; Section 4 details the TOKAMIND MMT architecture; Section 5 presents training and adaptation; Section 6 reports experimental results and ablations; and Section 7 provides concluding remarks and outlines future research directions.

## 2 Benchmark Overview: Data and Tasks

In this paper we employ TOKAMARK, a recently proposed benchmark designed to standardize the development and evaluation of AI models for fusion plasma dynamics [18]. Importantly, TOKAMARK moves beyond individual tasks and instead presents a suite of interconnected scientific objectives, meticulously curated to probe core capabilities required of AI models for fusion plasmas: (i) representation learning from complex and incomplete data; (ii) reasoning across diverse timescales; (iii) robustness to missing information; and (iv) generalization across operating regimes. From a technical point of view, TOKAMARK provides harmonized access to multi-modal diagnostics from MAST tokamak experiments and formalizes preprocessing steps such as temporal windowing, signal alignment, and metadata normalization. The use of TOKAMARK enables structured and reproducible training pipelines and, crucially, transparent and consistent comparison between different models. It also provides a strong baseline model and unified evaluation tooling, ensuring that new approaches can be benchmarked fairly.

and rigorously. For our purposes, we adhere to the taxonomy and protocols of TOKAMARK as closely as possible.

## 2.1 Data Summary

Based on the FAIR-MAST system and its associated MAST dataset [11, 12], TOKAMARK provides task-configured data loaders that provide streamlined access to the required diagnostics from the MAST tokamak. The benchmark includes diagnostic data for 11,573 *shots* (or *discharges*) of short duration—2–3 s long experiments, typical of tokamak operation—and makes available 39 signals spanning a range of diagnostic categories. These include magnetic measurements (flux loops, pickup coils, Mirnov coils), radiative diagnostics ( $D_\alpha$ , soft X-ray channels), kinetic measurements (Thomson scattering and interferometry), actuator commands (voltages applied to solenoid and poloidal field coils, gas fueling, neutral beam injection), and derived equilibrium quantities such as shape parameters, plasma boundaries,  $J_{\text{tor}}$  metrics, and flux maps.

In addition to physical categories, the signals are distinguished by their sampling frequency (ranging from 0.2 kHz up to 500 kHz) and structural shape, including:

- **time series**, represented as 1D tensors (scalar value over time);
- **profiles**, represented as 2D tensors (vector over time);
- **videos**, represented as 3D tensors (image over time).

Together, these heterogeneous signals form a rich, multi-rate, and multi-modal experimental dataset which, as any other, also contains gaps and noise.

## 2.2 Tasks Definition

TOKAMARK defines a suite of 14 supervised *window-to-window* learning tasks organized into 4 groups, each representing a broad scientific objective: instantaneous equilibrium reconstruction, fast magnetics dynamics, profile dynamics, and prediction of MHD activity. Each TOKAMARK task specifies three (possibly overlapping) sets of signals:

- an *input diagnostic set*  $I$  (sensor measurements),
- an optional *actuator set*  $A$  (machine control parameters), and
- an *output set*  $O$  (targets to be reconstructed or predicted),

together with a windowed sample defined by four times  $t_0 \leq t_1 \leq t_2 \leq t_3$ . Inputs are observed over the context window  $[t_0, t_1]$ , while outputs are defined over the target window  $[t_2, t_3]$ . When actuators are included, they are provided over  $[t_0, t_3]$ , covering both context and target horizon.

Depending on the objective, tasks fall into one of three families:

- reconstruction*:  $t_2 = t_0$  and  $t_3 = t_1$ , i.e., targets are defined on the same window as the inputs;
- autoregressive forecasting*:  $t_2 \geq t_1$  and  $t_3 > t_2$  with  $O \subseteq I$ , i.e., future values of (a subset of) input signals are predicted; and
- reconstructive forecasting*:  $t_2 \geq t_1$  and  $t_3 > t_2$  with outputs in  $O$  that may differ from  $I$ , i.e., related diagnostics or derived quantities are predicted over a future horizon.

Formally, each task can be described by the following window-to-window prediction problem:

$$\hat{y}_O([t_2, t_3]) = f_\theta(x_I([t_0, t_1]), u_A([t_0, t_3])).$$

In addition, TOKAMARK distinguishes *Markovian* and *non-Markovian* settings, depending on whether the target can be predicted from a short input window or if a longer temporal history is required.

For the formal descriptions of tasks, group-level organization, and full benchmark details, we refer the reader to [18].

## 3 TOKAMIND Tokenizer

The first step performed by TOKAMIND (see Fig. 1) is the tokenization process that converts windowed multi-modal signals with heterogeneous sampling rates into the model tokens. Given a windowed sample defined by  $(I, A, O)$  and both time windows  $[t_0, t_1]$  and  $[t_2, t_3]$ , tokenization produces a variable-length set of token embeddings  $\{z_i\}_{i=1}^L$ , where each token represents a chunk of signal data with  $L$  being the number of chunks used to decompose each window.

### 3.1 Transform Chain

For each window, tokenization proceeds through the following steps:

- (1) **Chunking**: Each input and actuator signal window is decomposed into fixed-duration chunks of length  $\Delta_{\text{chunk}}$  with stride  $s$  ( $s = \Delta_{\text{chunk}}$  for non-overlapping chunks). Chunking is a role-specific action: input chunks cover the window  $[t_0, t_1]$ , while actuator chunks may span a longer interval  $[t_0, t_3]$ . Output signals are *not* chunked. Also, chunking is based on fixed-size time intervals, so signals with different sampling rates contribute different numbers of samples per chunk while sharing the same chunk grid (and thus the same number of chunks prior to filtering). Chunks form the model’s base input elements and enable flexible context: the amount of history provided to the model is controlled by retaining more or fewer recent chunks, without changing the architecture.
- (2) **Filtering**: Chunks are filtered per signal and are marked as invalid if they are empty or contain non-numerical values. Windows are discarded if they do not contain at least one valid input/actuator and at least one valid output target. Optionally, windows are subsampled per shot by enforcing a minimum spacing in  $t_1$ . In order to bound the number of elements fed to the model, for each role we retain at most the  $M$  most recent valid chunks (i.e., those closest in time to the end of the prediction interval at  $t_3$ ).
- (3) **Embedding generation**: Each retained input/actuator chunk is transformed into a token embedding  $z_i \in \mathbb{R}^{K_{g(i)}}$  using a signal-specific embedding codec, where  $g(i)$  denotes the signal associated with the  $i$ -th token. Outputs are transformed at window level to provide supervision targets in the same embedding space.

After tokenization, each window yields: (i) a variable-length set of token embeddings  $\{z_i\}_{i=1}^L$  for the available input/actuator chunks, and (ii) window-level embedded targets for each output signal used for supervision, together with indicators of which outputs are present.

In the remainder of this section, we describe the embedding codecs  $E_g$  used to map native-rate chunks (and window-level outputs) into the shared embedding space.

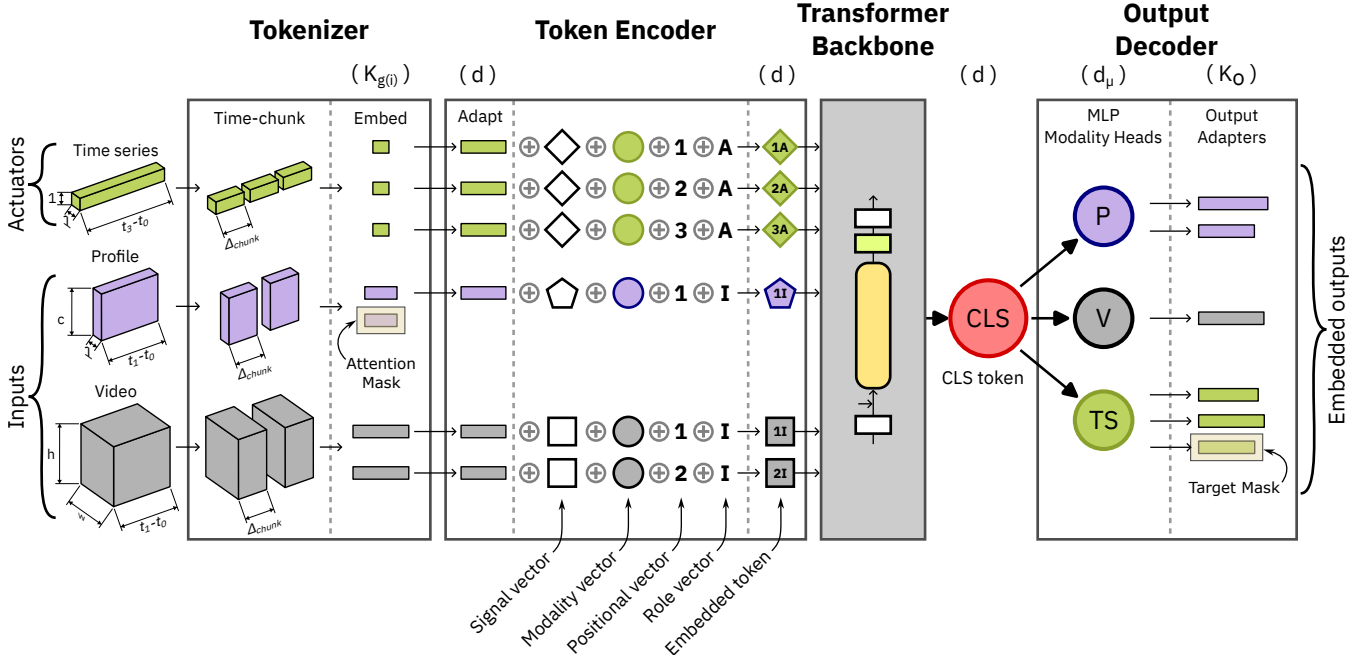


**Figure 1: TokaMind tokenization and model architecture.** Windowed multi-modal inputs  $I$  and actuators  $A$  are chunked and embedded by signal-specific codecs  $E_g$  to produce token embeddings  $z_i \in \mathbb{R}^{K_{g(i)}}$  (outputs are embedded at the window level to form targets in the same space). A Token Encoder projects each token to the shared model dimension  $d$  and adds learned metadata embeddings (signal, role, modality, relative position). A Transformer Backbone processes the variable-length token set using an attention mask for missing/padded tokens and outputs the [CLS] (classification) token embedding. Modality-specific heads (TS: time series, P: Profile, V: Video) and per-output adapters predict embedded targets  $\hat{y}_o \in \mathbb{R}^{K_o}$ ; a target-availability mask  $m_o$  excludes missing outputs from the supervised loss.

### 3.2 Chunk and Window Embedding

The embedding layer maps heterogeneous modalities into a common representation space, enabling a uniform token interface and a consistent supervision mechanism across tasks. For each signal  $g$ , we define an embedding codec  $E_g$  that maps an input chunk window (or an output window)  $x$  to a vector in  $\mathbb{R}^{K_g}$ . Applied to an input/actuator chunks, this yields a set of token embeddings  $z_i = E_{g(i)}(x_i) \in \mathbb{R}^{K_{g(i)}}$ , while output signals are embedded at the *window level* to form supervision targets  $y_o = E_o(x) \in \mathbb{R}^{K_o}$  in the same representation space.

Our default embedding choice is the training-free Discrete Cosine Transform codec (DCT3D) [3], used for pretraining and all downstream tasks. However, it is worth noting that the TOKAMIND framework is flexible and embedding-agnostic, and we additionally support identity embeddings (no compression) and learned embeddings produced by Variational Autoencoders (VAEs). As part of our experimental results in Section 6, we include the evaluation of VAE embeddings as an ablation on a subset of TOKAMIND tasks.

**3.2.1 DCT3D.** DCT3D, short for the three-dimensional discrete cosine transform [3], is a lightweight, training-free codec that compresses time-dependent signals by projecting them onto an orthonormal cosine basis over *space/channel* and *time*. A chunk (or output window) is represented as an array  $x$  that can be a 1D time-series, a 2D profile, or a 3D map/video. We treat all cases uniformly

by reshaping  $x$  to a 3D tensor  $x^{3D} \in \mathbb{R}^{H \times W \times T}$ , using singleton dimensions when needed (e.g.,  $(T) \rightarrow (1, 1, T)$  and  $(C, T) \rightarrow (C, 1, T)$ ). Let  $D_H \in \mathbb{R}^{H \times H}$ ,  $D_W \in \mathbb{R}^{W \times W}$ , and  $D_T \in \mathbb{R}^{T \times T}$  denote the orthonormal DCT-II bases along each axis. Applying the separable 3D DCT-II yields the coefficients tensor

$$C = \text{DCT}(x^{3D}) \in \mathbb{R}^{H \times W \times T},$$

and, equivalently,

$$\text{vec}(C) = (D_T \otimes D_W \otimes D_H) \text{ vec}(x^{3D}),$$

where function  $\text{vec}(\cdot)$  stacks tensor entries into a vector, with  $\otimes$  denoting the Kronecker product.

To form a compact representation, we retain only the low-frequency coefficients and define the truncated tensor  $\tilde{C} \in \mathbb{R}^{\tilde{H} \times \tilde{W} \times \tilde{T}}$  by

$$\tilde{C}_{hwt} = C_{hwt}, \quad 1 \leq h \leq \tilde{H}, 1 \leq w \leq \tilde{W}, 1 \leq t \leq \tilde{T}.$$

The final embedding of  $x$  is obtained by flattening  $\tilde{C}$ :

$$z = \text{vec}(\tilde{C}) \in \mathbb{R}^{K_g}, \quad K_g = \tilde{H} \cdot \tilde{W} \cdot \tilde{T}.$$

Reconstruction applies the inverse transform (IDCT) after zero-padding the missing DCT coefficients to recover  $\tilde{x}^{3D}$  with the original shape.

**Main benefits.** DCT3D provides three practical benefits. First, it yields a fixed-size embedding controlled by  $(\tilde{H}, \tilde{W}, \tilde{T})$ , enabling a uniform token representation across modalities and sampling patterns. Second, it is fast and requires no task-specific training,

since the cosine basis is fixed and data-independent; from this, new signals can be embedded without retraining the codec. Third, the orthonormal DCT preserves energy (by Parseval’s theorem), implying  $\|x^{3D}\|_2^2 = \|C\|_2^2$  i.e., the signal’s  $\ell_2$  norm can be computed directly from its DCT coefficients; consequently, the energy preserved by truncation is given by

$$\text{explained energy}(x^{3D}, z) = (\|x^{3D}\|_2^2)^{-1} \|z\|_2^2 \in [0, 1].$$

*Choosing the embedding dimension.* We select per-signal truncation sizes (and therefore  $K_g$ ) using the explained energy. In practice, for each signal we choose the smallest  $(\tilde{H}, \tilde{W}, \tilde{T})$  that reaches a target explained energy threshold, subject to a maximum number of coefficients budget  $K_{\max}$ .

**3.2.2 VAE.** As an alternative to our default training-free DCT3D embeddings, we also evaluate learned embeddings obtained by using variational autoencoders (VAEs) [16, 17] and trained for a subset of input signals required by the TOKAMARK tasks from *Group 1*.

In our framework, a VAE instantiates a signal-specific codec: the VAE encoder  $E_g$  maps a window/chunk  $x$  of signal  $g$  to a latent-space representation  $z \in \mathbb{R}^{K_g}$ . We set the latent dimensionality to approximately 10% of the input dimension, yielding a compact representation while preserving the relevant signal information.

The *codec encoder* is primarily a stack of one-dimensional convolutional layers; for a subset of low-dimensional time-series signals we instead employ fully connected (dense) layers. The *codec decoder* mirrors the codec encoder with reversed dimensionality, mapping latent vectors  $z$  back to reconstructions in the input space. VAEs are trained with the standard reconstruction-plus-regularization objective, and at inference time we use the codec-encoder output as the token embedding.

## 4 TOKAMIND Model

After the tokenization step is done, TOKAMIND maps a variable-length set of token embeddings  $\{z_i\}_{i=1}^L$  to predictions for a set of output targets. An overview of the model architecture is shown in Fig. 1. The model is organized into three components: (i) a *Token Encoder*, that maps each token embedding into a shared  $d$ -dimensional space and augments it with learned metadata lookup vectors; (ii) a *Transformer Processor*, that produces contextualized token representations; and (iii) an *Output Decoder*, that maps the pooled representation into target predictions. The Output Decoder is further decomposed into two blocks: *modality-specific MLP heads* and *per-target Output Adapters*, which provide the flexibility to support different output schemas across tasks.

### 4.1 Token Encoder

Each token corresponds to one embedded input/actuator chunk and consists of a content embedding  $z_i \in \mathbb{R}^{K_{g(i)}}$ ,  $i \in \{1, \dots, L\}$  together with discrete metadata: signal id  $g(i)$ , modality id  $\mu(i)$ , role id  $r(i)$ , and a relative position index  $p(i)$ . Let  $d$  denote the Transformer model dimension. The Token Encoder maps each token to a shared  $d$ -dimensional representation by (i) projecting the embedding vector with a signal-specific linear map, and (ii) adding learned lookup vectors for the discrete metadata:

$$h_i^{(0)} = W_{g(i)} z_i + e_{g(i)}^{\text{sig}} + e_{\mu(i)}^{\text{mod}} + e_{r(i)}^{\text{role}} + e_{p(i)}^{\text{pos}} \in \mathbb{R}^d,$$

where  $W_{g(i)}$  projects  $z_i$  into  $\mathbb{R}^d$  and  $e^{(\cdot)}$ , learnable  $d$ -dimensional vectors indexed by the token metadata.

Intuitively,  $e_{g(i)}^{\text{sig}}$  conditions the model on signal identity (and is used to define availability masks),  $e_{\mu(i)}^{\text{mod}}$  captures modality-specific structure,  $e_{r(i)}^{\text{role}}$  distinguishes sensors inputs from actuators, and  $e_{p(i)}^{\text{pos}}$  encodes position/recency. Relative positions are defined within each role by counting backwards from the newest retained chunk: the most recent chunk has  $p = 1$ , the next has  $p = 2$ , and so on. This provides a task-agnostic notion of recency and supports variable context lengths by changing only the number of retained chunks/tokens, without modifying the backbone.

We prepend a learnable [CLS] (classification) token embedding  $h_{\text{cls}}^{(0)} \in \mathbb{R}^d$  and form the initial transformer input

$$H^{(0)} = [h_{\text{cls}}^{(0)}, h_1^{(0)}, \dots, h_L^{(0)}] \in \mathbb{R}^{(L+1) \times d}$$

together with an attention mask that excludes padded or missing tokens. The final [CLS] embedding serves as a pooled window representation used by the Output Decoder.

### 4.2 Transformer Backbone

The Transformer processor follows a standard Transformer encoder architecture [21] that applies masked self-attention over the token sequence. It consists of  $N_{\text{layers}}$  stacked transformer blocks with multi-head self-attention and position-wise feed-forward layers, using residual connections and normalization. Self-attention is masked to exclude padded or missing tokens, enabling variable-length token sets.

Given the token-encoder output  $H^{(0)} \in \mathbb{R}^{(L+1) \times d}$ , each layer produces

$$H^{(\ell+1)} = \text{TransformerEnc}^{(\ell)}(H^{(\ell)}), \quad \ell = 0, \dots, N_{\text{layers}} - 1,$$

yielding contextualized representations  $H^{(N_{\text{layers}})}$ . We denote the final [CLS] embedding by  $c = H_{\text{cls}}^{(N_{\text{layers}})} \in \mathbb{R}^d$ , which serves as a pooled window representation for the Output Decoder.

### 4.3 Output Decoder

The Output Decoder maps the pooled window representation to predictions for each output target. It is structured in two stages: modality-specific MLP heads that produce latent representations, followed by per-target Output Adapters that map to the appropriate output embedding space.

**Modality Heads.** We obtain modality-specific latent representations from the pooled embedding  $c$ . For each modality  $\mu$  (e.g., time-series, profile, video), a lightweight MLP head  $\phi_\mu$  maps  $c$  to a modality latent

$$u_\mu = \phi_\mu(c) \in \mathbb{R}^{d_\mu},$$

with  $d_\mu = d$  in our experiments.

**Output Adapters.** Each target signal  $o \in O$  is predicted in its embedding space via an Output Adapter that maps from the corresponding modality latent to the target embedding dimension  $K_o$

$$\hat{y}_o = \psi_o(u_{\mu(o)}) \in \mathbb{R}^{K_o},$$

where  $\mu(o)$  denotes the modality of output  $o$ , and  $\psi_o$  is a small linear/MLP adapter.

**Outputs.** The model produces predictions  $\{\hat{y}_o\}_{o \in O}$  in the data embedding space. During evaluation, predictions are mapped back to native signal space using the corresponding decoding operator (e.g., IDCT for DCT3D, or a learned decoder for VAEs). Training losses and adaptation strategies (including warm-start and freezing policies) are described in the next section.

## 5 TOKAMIND Training and Adaptation

This section describes how TOKAMIND is trained and how a pre-trained model is adapted to new tasks and output schemas. We define the masked objective, summarize how missing inputs/targets are handled, and present our warm-start and freezing strategy.

### 5.1 Training Objective and Masking

We train TOKAMIND by comparing predictions and targets in the embedding space induced by the output codec. For each output signal  $o \in O$ , the model predicts an embedding vector  $\hat{y}_o \in \mathbb{R}^{K_o}$ . Preprocessing provides the corresponding target embedding  $y_o \in \mathbb{R}^{K_o}$  together with an availability mask  $m_o \in \{0, 1\}$  indicating whether  $o$  is present for the current window. We train with a masked mean-squared error over available targets

$$\mathcal{L} = \sum_{o \in O} \lambda_o m_o \frac{1}{K_o} \|\hat{y}_o - y_o\|_2^2, \quad (1)$$

where  $\lambda_o$  are optional per-output weights, and targets with  $m_o = 0$  do not contribute to the loss. An attention mask similarly excludes missing or padded tokens from self-attention.

Training in embedding space provides a uniform supervision interface across modalities and reduces the dimensionality of high-rate signals. Because supervision is provided in the embedded representation, achievable native-space accuracy is bounded by the embedding reconstruction error. Evaluation is performed in native space by applying the embedding-specific decoding operator. Alternatively, we may choose an identity codec for any output so that  $K_o$  equals the native dimensionality and the loss in Eq. (1) is computed directly in native space.

Optionally, training can be regularized by randomly dropping a subset of input/actuator tokens (or entire time chunks) and masking a subset of targets. As a result, TOKAMIND can be trained and evaluated on arbitrary subsets of available input modalities and target signals without requiring imputation or a fixed schema.

### 5.2 Warm-Start and Task Adaptation

We follow a two-stage protocol. First, we *pretrain* a single model on a broad mixture of signals/tasks in TOKAMARK to learn a general-purpose representation for tokamak plasma dynamics. Second, for each downstream task, we *fine-tune* a subset of model blocks together with task-specific Output Adapters (Section 6).

To adapt efficiently under task and schema variations (changes in  $I$ ,  $A$ ,  $O$ , or embedding dimensions), TOKAMIND supports warm-starting and (optionally) freezing the main model blocks, namely Token Encoder, Transformer Backbone, Modality Heads, and Output Adapters (Fig. 1). Warm-start uses partial loading: parameters are reused only when both their identifier and tensor shape match;

**Table 1: List of possible changes in the inputs and outputs between model runs and the corresponding adaptations.**

Change between runs	Model adaptation
Remove some inputs / actuators	✓ Fewer tokens; Transformer Backbone unchanged
Add new input / actuator	✓ New Token Encoder projection initialized; other blocks reused
Remove outputs	✓ Corresponding Output Adapters absent; loss ignores them via masks
Add new outputs	✓ New Output Adapters initialized; existing adapters reused
Change embedding dim / encoder for an existing signal	✓ Token Encoder / Output Adapter reinitialized (shape mismatch); other blocks reused
Change chunk length / max_chunks / stride	✓ Different token count; relative-position encoding preserves a consistent notion of recency
Evaluate on a subset of inputs/outputs	✓ Same masking mechanism; evaluation works on arbitrary subsets
Change $d$ (model dimension)	✗ Requires training a new Backbone / Backbone shape

mismatched or missing parameters remain at initialization. Consequently, common adaptation scenarios are handled predictably: adding a new input signal introduces a new projection layer in the token encoder while reusing the backbone; adding a new output introduces a new Output Adapter; changing an embedding dimension reinitializes only the affected projections/adapters; and changing the number of retained chunks affects sequence length at runtime without altering backbone parameters. Table 1 summarizes supported scenarios of changes and the resulting model behavior.

## 6 Experiments

### 6.1 Experimental Protocol

We evaluate two downstream regimes: task-specific *fine-tuning* of a pretrained Foundation Model (FM), and task-specific *training from scratch* under the same epoch budget. We first pretrain TOKAMIND on a broad multi-signal objective to obtain the initialization used for fine-tuning.

**FM pretraining.** We pretrain TOKAMIND on a broad signal set defined in our pretraining configuration. This pretrained checkpoint defines the *initialization reused for all downstream fine-tuning experiments*. Inputs include *all benchmark input diagnostics* and *all actuators* (16 sensor inputs and 5 actuators). Targets include *all benchmark inputs* and *all benchmark outputs* (34 targets). Pre-training uses a reconstruction objective on 50 ms windows. This broad multi-signal objective encourages the backbone to learn a general representation that transfers across tasks. We pretrain two model sizes, *Base* (9.32M parameters) and *Tiny* (5.29M parameters), to study the effect of model capacity. Notably, both variants remain lightweight, supporting efficient training and evaluation in this setting.

**Task-specific fine-tuning (warm-start).** For each downstream task, we initialize from the pretrained checkpoint and fine-tune in two

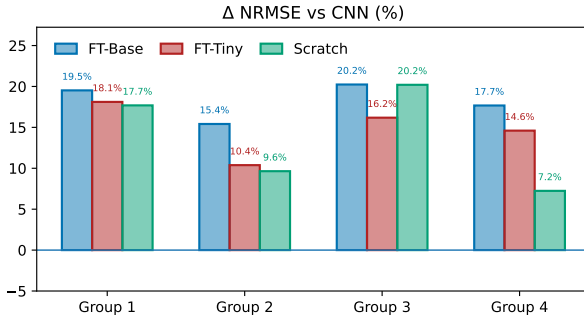


**Figure 2: Relative improvement in group-level test NRMSE over the CNN baseline on TokAMARK. Positive values indicate lower NRMSE (better) than the baseline; negative values indicate worse performance.**

stages. We warm-start the Token Encoder, Transformer Backbone, and Modality Heads; Output Adapters are instantiated per task since output sets and embedding dimensions are task-dependent. Stage 1 freezes the *Transformer Backbone* while updating the remaining task-facing components. Stage 2 freezes the *Token Encoder* and unfreezes the *Transformer Backbone*. Because each task uses only a subset of signals and parts of the network are frozen, fine-tuning updates substantially fewer parameters than end-to-end training.

*Training from scratch.* To isolate the benefit of pretraining, we also train task-specific TokAMIND models from random initialization. These models use the same epoch budget as the fine-tuned models and are trained independently for the 14 benchmark tasks.

*Embedding study.* We additionally perform a small embedding study on Group 1 tasks, comparing our default DCT3D embedding to a VAE-based embedding under the same downstream training protocol.

*Hyperparameters.* Exact model hyperparameters, optimization settings, and training schedules are reported in Appendix A.

## 6.2 Evaluation Protocol

We evaluate all models on the TokAMARK benchmark, following its task definitions, data splits, and evaluation protocol. We compare against the benchmark’s CNN baseline and report test-set performance using the benchmark’s normalized RMSE (NRMSE) aggregated per task and per group. Our models predict targets in embedding space; for evaluation, predictions are decoded to native signal space using the embedding-specific decoding operator and metrics are computed in native space. We refer the reader to the TokAMARK paper for the formal metric definitions and aggregation procedure.

## 6.3 Results

Per-task test NRMSE results are reported in Table 2, and group-level relative improvements over the CNN baseline are summarized in Fig. 2. Appendix Table A.1 reports signal-level results together with the corresponding DCT3D compression statistics for each output. We compare four methods: *CNN* (the TokAMARK baseline), *FT-Base* and *FT-Tiny* (TokAMIND fine-tuned per task from the pretrained Base and Tiny checkpoints), and *Scratch* (the Base

**Table 2: Test NRMSE on TokAMARK.** Best value per row is in bold. Group averages and overall average are unweighted means over tasks.

Group	Task	CNN	TokAMIND		
			FT-Base	FT-Tiny	Scratch
Group 1	1-1	0.1882	<b>0.1373</b>	0.1433	0.1387
	1-2	0.0482	0.0426	0.0440	<b>0.0417</b>
	1-3	0.2552	0.2157	<b>0.2153</b>	0.2242
	<i>Group 1 avg</i>	0.1639	<b>0.1319</b>	0.1342	0.1349
Group 2	2-1	0.1551	<b>0.1281</b>	0.1417	0.1482
	2-2	0.0517	0.0457	0.0478	<b>0.0450</b>
	2-3	0.1724	<b>0.1469</b>	0.1503	0.1494
	<i>Group 2 avg</i>	0.1264	<b>0.1069</b>	0.1133	0.1142
Group 3	3-1	0.3252	0.2941	0.3059	<b>0.2775</b>
	3-2	0.3309	<b>0.2802</b>	0.2952	0.2852
	3-3	0.3607	<b>0.2367</b>	0.2511	0.2487
	<i>Group 3 avg</i>	0.3389	<b>0.2703</b>	0.2841	0.2705
Group 4	4-1	0.3445	<b>0.2632</b>	0.2768	0.3202
	4-2	0.3311	<b>0.2618</b>	0.2732	0.3343
	4-3	0.2702	<b>0.0956</b>	0.1036	0.1397
	4-4	0.4292	<b>0.3325</b>	0.3687	0.3935
	4-5	<b>1.0053</b>	1.0065	1.0105	1.0203
<i>Group 4 avg</i>		0.4761	<b>0.3919</b>	0.4066	0.4416
<b>Overall avg</b>		0.3048	<b>0.2491</b>	0.2591	0.2690

TokAMIND trained per task from random initialization under a matched epoch budget).

*Main findings.* The major comparative results are listed below:

- **Consistent gains over the baseline:** both fine-tuned variants (*FT-Base* and *FT-Tiny*) outperform the CNN baseline on all but one task and across all four benchmark groups, indicating broad transfer across reconstruction and forecasting objectives.
- **Tiny model retains most of the performance:** *FT-Tiny* closely tracks *FT-Base* across groups with only minor degradations, suggesting that much of the benefit is retained at substantially lower capacity.
- **Pretraining helps most on harder tasks:** fine-tuning is generally stronger than training TokAMIND from scratch under a matched epoch budget, with the largest gap in Group 4 (longer-horizon, high-frequency targets). This is consistent with pretraining improving optimization stability and generalization in the most demanding settings, and suggests that it captures transferable representations of plasma dynamics.

*Edge case.* Task 4-5 remains the most challenging scenario: improvements are limited, and aggregate error is dominated by a small fraction of difficult windows (heavy-tailed per-window errors) for high-frequency (50 kHz) magnetic data. We verified the model can fit a small subset of shots (near-zero training error), suggesting the residual error is driven by rare regimes or outlier windows rather than a lack of model capacity. We therefore report Task 4-5 as a current limitation and leave it to further investigative work (including alternative preprocessing for high-frequency content).

**Table 3: Group 1 test NRMSE for VAE-based embeddings under FT-Base and Scratch regimes.  $\Delta$  reports the NRMSE difference to the corresponding DCT3D result from Table 2 under the same training regime.**

	VAE FT-Base		VAE Scratch	
	NRMSE	$\Delta$	NRMSE	$\Delta$
Group 1	Task 1-1	0.1501	+0.0129	0.1474 +0.0087
	Task 1-2	0.0544	+0.0118	0.0535 +0.0118
	Task 1-3	0.2507	+0.0350	0.2521 +0.0279
Avg		0.1517	+0.0198	0.1510 +0.0161

*Signal-level metrics.* At signal level (Appendix Table A.1), TOKAMIND improves over the CNN baseline on nearly all outputs. The only exception is `equilibrium-x_point_z` (the vertical position of the X-point), with the CNN baseline being better in both Task 1-1 (no compression) and in Task 2-1, where DCT3D retains only a subset of temporal coefficients (2 out of 5). In general, DCT3D acts as an identity (or near-identity) mapping for many low-dimensional equilibrium scalars, while providing substantial compression for higher-dimensional and high-rate targets at high explained variance; the most challenging long-horizon, namely high-frequency coil targets (Task 4-5), require the largest budgets and exhibit the lowest explained variance under our fixed budget cap.

*Embedding study: DCT3D vs VAE.* We conduct a focused embedding study on Group 1 to compare our default, training-free DCT3D embedding against a learned VAE embedding. VAE codecs are pre-trained on MAST data using all Task 1 input signals. Task 1 outputs contain only a single sample within the output horizon; we therefore use an identity codec for outputs (loss in native space) and compute the loss directly in native space. We compare DCT3D and VAE under the same downstream training protocol, considering both training from scratch and task-specific fine-tuning. Since fine-tuned models are warm-started from a DCT3D-pretrained checkpoint, this initialization may be suboptimal for VAE-based embeddings; therefore, training from scratch provides the fairest assessment of the embedding choice.

VAE results for Group 1, together with their  $\Delta$  relative to the corresponding DCT3D models, are reported in Table 3. Appendix Table A.2 reports the corresponding input shapes and DCT3D/VAE embedding dimensions. Overall, DCT3D performs slightly better than the VAE variants in this setting, indicating that a simple frequency-based representation is already competitive for these signals and horizons. At the same time, the VAE achieves close performance to DCT3D and still outperforms the benchmark baseline; moreover, Appendix Table A.2 shows that VAE embeddings are often more compressed than DCT3D for the Group 1 inputs (higher  $\text{dim}/K_g$ ). This suggests that learned embeddings are a promising direction; we expect further gains from a dedicated learned-embedding study (e.g., VAE-specific pretraining initializations, objectives, and hyperparameter tuning), which we leave to future work.

## 7 Conclusions

TOKAMIND is a modular, multi-modal transformer designed for tokamak data, data that is characterized by heterogeneous modalities, multi-rate sampling, and partial observability. TOKAMIND tokenizes windowed diagnostics and actuators into a variable-length set of token embeddings, and processes them with a shared Transformer Backbone. A two-stage Output Decoder composed of Modality-specific Heads and per-target Output Adapters enables flexible prediction across tasks with heterogeneous objectives and output schemas, while explicit masks support missing inputs and targets without the need of imputation actions.

On the TOKAMARK benchmark, TOKAMIND consistently improves over the CNN baseline across all tasks and groups. Warm-start fine-tuning from a pretrained checkpoint generally outperforms training from scratch, with the largest gains on the most challenging long-horizon and high-frequency tasks. These results support the foundation-model perspective: broad multi-signal pretraining effectively yields a transferable initialization that learns reusable representations of plasma dynamics. A pretrained, schema-flexible model can therefore serve as a reusable representation that accelerates data-driven tools across tasks and operating regimes.

Future work will focus on extending TOKAMIND beyond MAST to other tokamaks and reactor settings, enabling broader cross-device generalization by exploiting its modular design and schema-flexible tokenization. Another direction is a more extensive study of embedding choices—including learned codecs and task-adaptive representations—which may further improve performance, particularly for high-frequency targets. We also plan to investigate the integration of pretrained PDE foundation models as physics-aware priors for plasma dynamics, to assess whether such models [9] can improve data efficiency and long-horizon forecasting when combined with multi-modal fusion. Beyond plasma fusion, the proposed tokenization framework is applicable to many multi-channel scientific problems with heterogeneous sensors, missing channels, and varying schemas.

## References

- [1] Rushil Anirudh, Rick Archibald, M Salman Asif, Markus M Becker, Sadruddin Benkadda, Peer-Timo Bremer, Rick HS Bude, Choong-Seock Chang, Lei Chen, RM Churchill, et al. 2023. 2022 review of data-driven plasma science. *IEEE Transactions on Plasma Science* 51, 7 (2023), 1750–1838.
- [2] Muhammad Awais, Muzammal Naseer, Salman Khan, Rao Muhammad Anwer, Hisham Cholakkal, Mubarak Shah, Ming-Hsuan Yang, and Fahad Shahbaz Khan. 2025. Foundation models defining a new era in vision: a survey and outlook. *IEEE Transactions on Pattern Analysis and Machine Intelligence* (2025).
- [3] Said Boussakta and Hamoud O Alshibami. 2004. Fast algorithm for the 3-D DCT-II. *IEEE Transactions on Signal Processing* 52, 4 (2004), 992–1001.
- [4] R Michael Churchill. 2025. AI foundation models for experimental fusion tasks. *Frontiers in Physics* 12 (2025), 1531334.
- [5] AE Costley, DJ Campbell, S Kasai, KE Young, and V Zaveriaev. 2001. ITER R&D: auxiliary systems: plasma diagnostics. *Fusion Engineering and Design* 55, 2-3 (2001), 331–346.
- [6] Jonas Degrave, Federico Felici, Jonas Buchli, Michael Neunert, Brendan Tracey, Francesco Carpanese, Timo Ewalds, Roland Hafner, Abbas Abdolmaleki, Diego de Las Casas, et al. 2022. Magnetic control of tokamak plasmas through deep reinforcement learning. *Nature* 602, 7897 (2022), 414–419.
- [7] Nanyi Fei, Zhiwu Lu, Yizhao Gao, Guoxing Yang, Yuqi Huo, Jingyuan Wen, Haoyu Lu, Ruihua Song, Xin Gao, Tao Xiang, et al. 2022. Towards artificial general intelligence via a multimodal foundation model. *Nature Communications* 13, 1 (2022), 3094.
- [8] F Felici and O Sauter. 2012. Non-linear model-based optimization of actuator trajectories for tokamak plasma profile control. *Plasma Physics and Controlled Fusion* 54, 2 (2012), 025002.

[9] Maximilian Herde, Bogdan Raonic, Tobias Rohner, Roger Käppeli, Roberto Molinaro, Emmanuel De Bezenac, and Siddhartha Mishra. 2024. Poseidon: Efficient foundation models for pdes. *Advances in Neural Information Processing Systems* 37 (2024), 72525–72624.

[10] David Humphreys, Ana Kupresanin, Mark D Boyer, John Canik, CS Chang, Eric C Cyr, Robert Granetz, Jeffrey Hittinger, Egemen Kolemen, Earl Lawrence, et al. 2020. Advancing fusion with machine learning research needs workshop report. *Journal of Fusion Energy* 39, 4 (2020), 123–155.

[11] Samuel Jackson, Saiful Khan, Nathan Cummings, James Hodson, Shaun de Witt, Stanislas Pamela, Rob Akers, and Jeyan Thiyanagalingam. 2025. An Open Data Service for Supporting Research in Machine Learning on Tokamak Data. *IEEE Transactions on Plasma Science* (2025). doi:10.1109/TPS.2025.3583419

[12] Samuel Jackson, Saiful Khan, Nathan Cummings, James Hodson, Shaun de Witt, Stanislas Pamela, Rob Akers, Jeyan Thiyanagalingam, and The MAST Team. 2024. FAIR-MAST: A fusion device data management system. *SoftwareX* 27 (2024), 101869.

[13] Azarakhsh Jalalvand, SangKyeun Kim, Jaemin Seo, Qiming Hu, Max Curie, Peter Steiner, Andrew Oakleigh Nelson, Yong-Su Na, and Egemen Kolemen. 2025. Multimodal super-resolution: discovering hidden physics and its application to fusion plasmas. *Nature communications* 16, 1 (2025), 8506.

[14] Semin Joung, Y-C Ghim, Jaewook Kim, Sehyun Kwak, Daeho Kwon, C Sung, D Kim, Hyun-Seok Kim, JG Bak, and SW Yoon. 2023. GS-DeepNet: mastering tokamak plasma equilibria with deep neural networks and the Grad-Shafranov equation. *Scientific Reports* 13, 1 (2023), 15799.

[15] Minseok Kim, SangKyeun Kim, Andrew Rothstein, Peter Steiner, Keith Erickson, Young-Ho Lee, Hyunsun Han, Sang-hee Hahn, June-woo Juhn, Boseong Kim, et al. 2026. Real-time reconstruction and control of pedestal-top electron density using RMP and gas puff at KSTAR. *Plasma Physics and Controlled Fusion* 68, 1 (2026), 015007.

[16] Diederik P Kingma and Max Welling. 2013. Auto-Encoding Variational Bayes. *arXiv preprint* (2013). arXiv:1312.6114 [stat.ML]

[17] Simon J.D. Prince. 2023. *Understanding Deep Learning*. The MIT Press. <http://udlbook.com>

[18] Cécile Rousseau, Samuel Jackson, Rodrigo H. Ordóñez-Hurtado, Nicola C. Amorisco, Tobia Boschi, George K. Holt, Andrea Loreti, Eszter Székely, Alexander Whittle, Adriano Agnello, Stanislas Pamela, Alessandra Pascale, Robert Akers, Juan Bernabe Moreno, Sue Thorne, and Mykhaylo Zayats. 2026. TokaMark: A Comprehensive Benchmark for MAST Tokamak Plasma Models. *arXiv preprint* (2026). arXiv:2602.10132 [physics.plasm-ph]

[19] Ricardo Shousha, Jaemin Seo, Keith Erickson, Zichuan Xing, SangKyeun Kim, Joseph Abbate, and Egemen Kolemen. 2023. Machine learning-based real-time kinetic profile reconstruction in DIII-D. *Nuclear Fusion* 64, 2 (2023), 026006.

[20] U.S. Department of Energy. 2025. *Fusion Science & Technology Roadmap*. Technical Report. U.S. Department of Energy. <https://www.energy.gov/sites/default/files/2025-10/fusion-s%26t-roadmap-101625.pdf>

[21] Ashish Vaswani, Noam Shazeer, Niki Parmar, Jakob Uszkoreit, Llion Jones, Aidan N Gomez, Łukasz Kaiser, and Illia Polosukhin. 2017. Attention is all you need. *Advances in neural information processing systems* 30 (2017).

[22] Michael L Walker, Peter De Vries, Federico Felici, and Eugenio Schuster. 2020. Introduction to tokamak plasma control. In *2020 American Control Conference (ACC)*. IEEE, 2901–2918.

[23] Wei Zheng, Fengming Xue, Zhongyong Chen, Dalong Chen, Bihao Guo, Chengshuo Shen, Xinkun Ai, Nengchao Wang, Ming Zhang, Yonghua Ding, et al. 2023. Disruption prediction for future tokamaks using parameter-based transfer learning. *Communications Physics* 6, 1 (2023), 181.

## A Hyperparameters and Implementation Details

### A.1 DCT3D tuning

We tune DCT3D’s truncation parameters by selecting the smallest coefficient budget that reaches a target explained-energy threshold. Tuning is performed on a fixed subset of 100 shots and uses a coarser window sampling stride than training (stride=0.02 s) to reduce redundancy. Table A.1 reports the tuned DCT3D settings used for all outputs across tasks, while Table A.2 reports the corresponding settings for Group 1 inputs.

For pretraining, we tune input, actuator, and output encoders jointly with role-specific thresholds: 0.999 for inputs and actuators, and 0.995 for outputs. We cap the pretraining embedding budget at  $K_{\max}^{\text{pre}} = 4096$ .

For downstream tasks (fine-tuning and scratch), we reuse the same input/actuator chunk representation (5 ms chunks) and re-tune *outputs only* with a stricter threshold (0.999), setting the maximum budget to  $K_{\max} = 9,216$ . In practice, this larger budget is required only for a small subset of high-frequency, long-horizon tasks (Tasks 3-3, 4-1, 4-2, and 4-5). For example, in Task 4-5, the output horizon is 100 ms, and our tuned DCT3D output embedding retains up to  $3 \times 3072 = 9,216$  coefficients for the magnetic coil targets.

For Task 1-1, the output horizon contains a single sample per target; we therefore use an identity codec (no encoding/decoding), i.e., we compute the loss directly in native space.

## A.2 Model Architectures

We report two pretrained model sizes: *Base* (9,324,382 parameters) and *Tiny* (5,293,854 parameters). Both use the same modular structure described in Section 4, with them differing only in Transformer Backbone capacity (e.g.,  $d$ , number of layers/heads, FF dimension).

For the *Base* model, the Transformer Backbone uses  $d = 192$ , 4 layers, 6 heads, FF dimension 768, and dropout 0.05, with ReLU activation. For the *Tiny* model, the Transformer Backbone uses  $d = 128$ , 2 layers, 4 heads, FF dimension 384, and dropout 0.05, with ReLU activation. Modality Heads use per-modality MLPs with hidden dimension and output dimension  $d$ .

*Output Adapter policy.* Pretraining uses linear Output Adapters, while downstream fine-tuned/scratch runs enable bucketed hidden dimensions for Output Adapters based on output embedding size. Concretely, we use the following bucket rules in downstream runs: outputs with embedding dimension  $\leq 64$  use hidden size 0,  $\leq 512$  use 32,  $\leq 4096$  use 64,  $\leq 8192$  use 128, and larger outputs use hidden size  $d$ .

## A.3 Training Hyperparameters

All models are trained with *AdamW* and automatic mixed precision (AMP). We use early stopping with patience 10 and  $\Delta = 0$ . Learning-rate schedules use a warmup fraction of 0.02.

*Pretraining.* Pretraining is run for 50 epochs. We use per-block learning rates: Token Encoder  $5 \times 10^{-3}$ , Transformer Backbone  $10^{-3}$ , Modality Heads  $5 \times 10^{-3}$ , and Output Adapters  $5 \times 10^{-3}$ . Learning-rate schedules use a linear warmup over the first 2% of training steps, followed by cosine decay to zero over the remaining steps. The batch size is 512 windows.

*Fine-tuning (two stages).* Fine-tuning proceeds in two stages: 5 epochs with the Transformer Backbone frozen, followed by 15 epochs with the Token Encoder frozen. Stage-specific learning rates are:

- *Stage 1 (Backbone frozen):* Token Encoder  $5 \times 10^{-4}$ , Modality Heads  $10^{-3}$ , Output Adapters  $5 \times 10^{-3}$ .
- *Stage 2 (Token Encoder frozen):* Transformer Backbone  $5 \times 10^{-4}$ , Modality Heads  $10^{-3}$ , Output Adapters  $5 \times 10^{-3}$ .

Weight decay is 0.01 on the trainable blocks in each stage. Fine-tuning uses a batch size of 512 windows for all tasks, except Group 4 tasks where we use 256 due to higher memory requirements.

*Windowing, chunking, and collation.* All experiments use nonoverlapping 5 ms chunks and retain up to 50 chunks per role (inputs and actuators). In non-Markovian tasks—where the full shot history is in principle available—we cap the context to the most recent 150 ms of inputs and predict over a 100 ms horizon; with 5 ms chunking, this corresponds to 30 input chunks and 20 horizon-aligned chunks, and actuators are supplied over the extended input+output window. To reduce redundancy, we subsample candidate windows (stride 5 ms for Groups 1–2, 10 ms for Group 3, and 20 ms for Group 4), then pad each batch to the maximum token length with attention masks; we also apply per-token and per-chunk dropout during collation to improve robustness to missing diagnostics.

*Training from scratch.* Scratch runs follow the same architecture as the Base fine-tuned model, and use the same epoch budget as fine-tuning (20 epochs).

#### A.4 Computational Resources

All experiments were run on a single GPU node equipped with an NVIDIA A100-SXM4-80GB GPU (80 GB VRAM) with CUDA 12.8 (driver 570.195.03). To amortize preprocessing cost, we cache window-level representations in memory; caching uses `float16` storage and 32 worker processes for cache materialization.

**Table A.1: Detailed per-signal test NRMSE in native space (expanded view of Table 2). DCT3D columns summarize the output codec: native tensor shape  $(H, W, T)$ , retained coefficients  $(\tilde{H}, \tilde{W}, \tilde{T})$ , embedding dimension  $K_g$ , compression ratio  $\dim/K_g$  with  $\dim = HWT$ , and explained variance (rounded to 3 decimals). Model columns then report NRMSE for the CNN baseline and TOKAMIND variants (FT-Base, FT-Tiny, Scratch). Best NRMSE per row is in bold.**

Group	Task	Signal	DCT3D					Model NRMSE			
			$(H, W, T)$	$(\tilde{H}, \tilde{W}, \tilde{T})$	$K_g$	$\dim/K_g$	Expl. var.	CNN	FT-Base	FT-Tiny	Scratch
Group 1	1-1	equilibrium-beta_normal	(1, 1, 1)	(1, 1, 1)	1	1	1.000	0.2734	<b>0.2088</b>	0.2254	0.2098
		equilibrium-beta_pol	(1, 1, 1)	(1, 1, 1)	1	1	1.000	0.2668	0.2013	0.2154	<b>0.2009</b>
		equilibrium-beta_tor	(1, 1, 1)	(1, 1, 1)	1	1	1.000	0.2415	<b>0.1846</b>	0.2000	0.1907
		equilibrium-bphi_rmag	(1, 1, 1)	(1, 1, 1)	1	1	1.000	0.1497	<b>0.0908</b>	0.0969	0.0988
		equilibrium-bvac_rmag	(1, 1, 1)	(1, 1, 1)	1	1	1.000	0.1367	<b>0.0823</b>	0.0874	0.0923
		equilibrium-elongation	(1, 1, 1)	(1, 1, 1)	1	1	1.000	0.2342	0.1733	0.1797	<b>0.1719</b>
		equilibrium-elongation_axis	(1, 1, 1)	(1, 1, 1)	1	1	1.000	0.2676	0.1893	0.1967	<b>0.1885</b>
		equilibrium-magnetic_axis_r	(1, 1, 1)	(1, 1, 1)	1	1	1.000	0.1557	0.1291	0.1316	<b>0.1266</b>
		equilibrium-magnetic_axis_z	(1, 1, 1)	(1, 1, 1)	1	1	1.000	0.1429	<b>0.0907</b>	0.0934	0.0918
		equilibrium-minor_radius	(1, 1, 1)	(1, 1, 1)	1	1	1.000	0.1805	0.1554	0.1580	<b>0.1521</b>
Group 2	2-1	equilibrium-q95	(1, 1, 1)	(1, 1, 1)	1	1	1.000	0.1749	<b>0.1196</b>	0.1259	0.1294
		equilibrium-triangularity_lower	(1, 1, 1)	(1, 1, 1)	1	1	1.000	0.2277	0.1766	0.1776	<b>0.1738</b>
		equilibrium-triangularity_upper	(1, 1, 1)	(1, 1, 1)	1	1	1.000	0.2155	<b>0.1737</b>	0.1795	0.1749
		equilibrium-x_point_r	(2, 1, 1)	(2, 1, 1)	2	1	1.000	0.1431	0.0619	0.0617	<b>0.0587</b>
		equilibrium-x_point_z	(2, 1, 1)	(2, 1, 1)	2	1	1.000	<b>0.0130</b>	0.0218	0.0200	0.0210
		equilibrium-lcfs_r	(170, 1, 1)	(16, 1, 1)	16	10.62	1.000	0.0559	0.0462	0.0481	<b>0.0449</b>
		equilibrium-lcfs_z	(170, 1, 1)	(16, 1, 1)	16	10.62	0.999	0.0404	0.0391	0.0398	<b>0.0384</b>
		equilibrium-psi	(65, 65, 1)	(32, 16, 1)	512	8.25	0.999	0.2552	0.2157	<b>0.2153</b>	0.2242
		equilibrium-beta_normal	(1, 1, 5)	(1, 1, 5)	5	1	1.000	0.2301	<b>0.2067</b>	0.2327	0.2424
		equilibrium-beta_pol	(1, 1, 5)	(1, 1, 5)	5	1	1.000	0.2252	<b>0.1942</b>	0.2136	0.2202
Group 3	3-1	equilibrium-beta_tor	(1, 1, 5)	(1, 1, 5)	5	1	1.000	0.2158	<b>0.1927</b>	0.2240	0.2307
		equilibrium-bphi_rmag	(1, 1, 5)	(1, 1, 5)	5	1	1.000	0.1152	<b>0.0935</b>	0.1004	0.1113
		equilibrium-bvac_rmag	(1, 1, 5)	(1, 1, 5)	5	1	1.000	0.1079	<b>0.0812</b>	0.0914	0.0965
		equilibrium-elongation	(1, 1, 5)	(1, 1, 5)	5	1	1.000	0.2147	<b>0.1861</b>	0.1975	0.2114
		equilibrium-elongation_axis	(1, 1, 5)	(1, 1, 5)	5	1	1.000	0.2527	<b>0.2066</b>	0.2198	0.2321
		equilibrium-magnetic_axis_r	(1, 1, 5)	(1, 1, 5)	5	1	1.000	0.1462	<b>0.1335</b>	0.1499	0.1586
		equilibrium-magnetic_axis_z	(1, 1, 5)	(1, 1, 5)	5	1	1.000	0.1393	<b>0.1078</b>	0.1156	0.1244
		equilibrium-minor_radius	(1, 1, 5)	(1, 1, 5)	5	1	1.000	0.1677	<b>0.1562</b>	0.1687	0.1764
		equilibrium-q95	(1, 1, 5)	(1, 1, 5)	5	1	1.000	0.1514	<b>0.1237</b>	0.1379	0.1451
		equilibrium-triangularity_lower	(1, 1, 5)	(1, 1, 5)	5	1	1.000	0.2187	<b>0.1901</b>	0.2046	0.2084
Group 4	4-1	equilibrium-triangularity_upper	(1, 1, 5)	(1, 1, 5)	5	1	1.000	0.2093	<b>0.1885</b>	0.2027	0.2087
		equilibrium-x_point_r	(2, 1, 5)	(2, 1, 4)	8	1.25	0.999	0.1272	<b>0.0781</b>	0.0931	0.0962
		equilibrium-x_point_z	(2, 1, 5)	(2, 1, 2)	4	2.50	1.000	<b>0.0122</b>	0.0210	0.0304	0.0378
		pf_active-coil_current	(10, 1, 100)	(10, 1, 8)	80	12.50	1.000	0.1057	<b>0.0604</b>	0.0706	0.0676
		pf_active-solenoid_current	(1, 1, 100)	(1, 1, 4)	4	25	1.000	0.0726	<b>0.0298</b>	0.0314	0.0339
		summary-ip	(1, 1, 100)	(1, 1, 16)	16	6.25	0.999	0.0803	<b>0.0550</b>	0.0657	0.0652
		equilibrium-lcfs_r	(170, 1, 5)	(16, 1, 2)	32	26.56	0.999	0.0561	0.0479	0.0505	<b>0.0472</b>
		equilibrium-lcfs_z	(170, 1, 5)	(16, 1, 4)	64	13.28	0.999	0.0473	0.0435	0.0452	<b>0.0429</b>
		equilibrium-psi	(65, 65, 5)	(32, 16, 5)	2560	8.25	0.999	0.1724	<b>0.1469</b>	0.1503	0.1494
		thomson_scattering-n_e	(120, 1, 10)	(120, 1, 10)	1200	1	1.000	0.3307	0.2933	0.3069	<b>0.2749</b>
Group 3	3-2	thomson_scattering-t_e	(120, 1, 10)	(120, 1, 10)	1200	1	1.000	0.3196	0.2950	0.3049	<b>0.2802</b>
		soft_x_rays-horizontal_cam_lower	(18, 1, 2500)	(18, 1, 512)	9216	4.88	0.993	0.2382	<b>0.2034</b>	0.2077	0.2092
		soft_x_rays-horizontal_cam_upper	(18, 1, 2500)	(18, 1, 512)	9216	4.88	0.988	0.2717	<b>0.2255</b>	0.2362	0.2365
		spectrometer_visible-filter_spectrometer_dalpha_voltage	(3, 1, 2500)	(3, 1, 1024)	3072	2.44	0.999	0.4830	0.4118	0.4418	<b>0.4099</b>
		equilibrium-beta_normal	(1, 1, 1)	(1, 1, 1)	1	1	1.000	0.3256	<b>0.2195</b>	0.2327	0.2403
		equilibrium-beta_pol	(1, 1, 1)	(1, 1, 1)	1	1	1.000	0.3028	<b>0.2177</b>	0.2303	0.2339
		equilibrium-beta_tor	(1, 1, 1)	(1, 1, 1)	1	1	1.000	0.2865	<b>0.1777</b>	0.1986	0.1919
		thomson_scattering-n_e	(120, 1, 1)	(120, 1, 1)	120	1	1.000	0.5143	<b>0.2896</b>	0.3047	0.2925
		thomson_scattering-t_e	(120, 1, 1)	(120, 1, 1)	120	1	1.000	0.3744	<b>0.2788</b>	0.2892	0.2848
		soft_x_rays-horizontal_cam_lower	(18, 1, 5000)	(18, 1, 512)	9216	9.77	0.990	0.3184	<b>0.2442</b>	0.2553	0.2962
Group 4	4-2	soft_x_rays-horizontal_cam_upper	(18, 1, 5000)	(18, 1, 512)	9216	9.77	0.985	0.3705	<b>0.2821</b>	0.2984	0.3442
		soft_x_rays-horizontal_cam_lower	(18, 1, 5000)	(18, 1, 512)	9216	9.77	0.990	0.3215	<b>0.2430</b>	0.2540	0.3138
		soft_x_rays-horizontal_cam_upper	(18, 1, 5000)	(18, 1, 512)	9216	9.77	0.985	0.3406	<b>0.2806</b>	0.2923	0.3548
		equilibrium-magnetic_axis_z	(1, 1, 20)	(1, 1, 20)	20	1	1.000	0.2702	<b>0.0956</b>	0.1036	0.1397
		summary-ip	(1, 1, 400)	(1, 1, 32)	32	12.50	0.999	0.4292	<b>0.3325</b>	0.3687	0.3935
Group 4	4-3	magnetics-b_field_pol_probe_omv_voltage	(3, 1, 50000)	(3, 1, 3072)	9216	16.28	0.633	0.9371	<b>0.9368</b>	0.9376	0.9380
		magnetics-b_field_tor_probe_cc_field	(3, 1, 50000)	(3, 1, 3072)	9216	16.28	0.723	<b>1.0734</b>	1.0762	1.0833	1.1026

**Table A.2: Group 1 input signals.**  $(H, W, T)$  denotes the native tensor shape for a single 5 ms chunk, with  $\text{dim} = HWT$ . DCT3D columns report tuned coefficient retention  $(\tilde{H}, \tilde{W}, \tilde{T})$ , effective embedding dimension  $K_g$  (product of retained coefficients), compression ratio  $\text{dim}/K_g$ , and explained variance. VAE columns report the latent embedding dimension  $K_g$  and the corresponding compression ratio  $\text{dim}/K_g$ .

Signal	(H, W, T)	DCT3D				VAE	
		$(\tilde{H}, \tilde{W}, \tilde{T})$	$K_g$	$\text{dim}/K_g$	Expl. var.	$K_g$	$\text{dim}/K_g$
magnetics-flux_loop_flux	(15, 1, 25)	(15, 1, 1)	15	25.00	0.9994	12	31.25
magnetics-b_field_pol_probe_ccbv_field	(40, 1, 25)	(40, 1, 2)	80	12.50	0.9994	30	33.33
magnetics-b_field_pol_probe_обр_field	(18, 1, 25)	(18, 1, 2)	36	12.50	0.9992	15	30.00
magnetics-b_field_pol_probe_obv_field	(18, 1, 25)	(18, 1, 2)	36	12.50	0.9996	15	30.00
magnetics-b_field_tor_probe_saddle_voltage	(12, 1, 250)	(12, 1, 1)	12	250.00	0.9992	8	375.00
pf_active-coil_current	(10, 1, 20)	(10, 1, 2)	20	10.00	0.9996	6	33.33
pf_active-solenoid_current	(1, 1, 20)	(1, 1, 2)	2	10.00	0.9997	4	5.00
summary-ip	(1, 1, 20)	(1, 1, 4)	4	5.00	0.9991	3	6.67